PCCP

Accepted Manuscript

This is an *Accepted Manuscript*, which has been through the Royal Society of Chemistry peer review process and has been accepted for publication.

Accepted Manuscripts are published online shortly after acceptance, before technical editing, formatting and proof reading. Using this free service, authors can make their results available to the community, in citable form, before we publish the edited article. We will replace this *Accepted Manuscript* with the edited and formatted *Advance Article* as soon as it is available.

You can find more information about *Accepted Manuscripts* in the **Information for Authors**.

Journal Name

RSC**Publishing**

COMMUNICATION

Integrated SnO₂ Nanorod Array with Polypyrrole Coverage for High-rate and Long-life Lithium Batteries

Lei Zhang[§], Kangning Zhao[§], Wangwang Xu[§], Yifan Dong, Rui Xia, Fengning Liu, Liang He*, Qiulong Wei, Mengyu Yan, Liqiang Mai*

State Key Laboratory of Advanced Technology for Materials Synthesis and Processing, WUT-Harvard Joint Nano Key Laboratory, Wuhan University of Technology, Wuhan 430070, China

Conversion/alloying reactions based on more lithium ion involved in the reaction are severely handicapped by the dramatic volume changes. A facile and versatile strategy has been developed for integrating the SnO₂ nanorod array in the PPy nanofilm for providing a flexible confinement for anchoring each nanorod and maintaining the whole structural integrity and providing sustainable contract, therefore, exhibiting much more stable cycling stability (701 mAh/g after 300 cycles) and better high-rate capability (512 mAh/g at 3 A/g) when compared with the core-shell SnO₂-PPy NA.

Introduction

Concerns over limited energy resources, as well as the need to decrease greenhouse gas emissions, have stimulated the demands to apply renewable energy resouces at a large scale, along with the widespread application of hybrid and electric vehicles[1-4]. Among the various energy conversion/storage systems proposed, lithium ion battery is very well positioned to satisfy these needs, but research towards high capacity and high rate capability is still imperious[5-10]. Progress in the study of insertion compounds enabled the development and commercialisation of lithium ion batteries, but a paradigmatic shift in energy density will only be achieved with the use of electrodes operating through alternative reaction mechanisms, namely the conversion reaction and the alloy reaction, allowing for more electrons per atom ultilized which are associated with much higher energy densities than that of insertion reactions[11-16].

Among them, SnO₂ attracts particular attention due to the high theoretical capacity and safe working potential[23-25]. The high theoretical capacity is orignated from a two-step reaction that SnO₂ generally is regarded to witness [26]:

$$SnO_2 + 4Li^+ + 4e^- = Sn + 2Li_2O$$

$$Sn + 4.4Li^+ + 4.4e^- = Li_{4.4}Sn$$
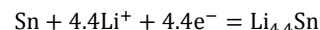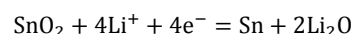
The initial process is conversion reaction, yielding tin particle and Li₂O, which is generally regarded as irreversible[27]. The following alloying process is widely known to be reversible and 4.4 mol lithium ions can be reversiblely alloyed and dealloyed with Sn, resulting in the large volume expansion–contraction (~300%)[28]. The huge voulumic variation is generally reagarded as the result of severe capacity fading. Due to the two-step reaction above, more lithium ions are induced into the host structure, bringing about higher volume expansion upon cycling, leading to the disintegration and pulversization of the electrode, resulting in the continuous breakdown and frequent formation of a very thick solid electrolyte interphase (SEI) and consumption of the electrolyte[29]. Therefore, rational design should be taken into account all of the above considerations to improve the cycle performance of SnO₂.
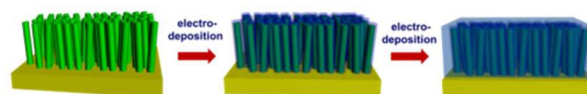

Figure 1. schematic illustration of the formation process of the SnO₂-PPy nanofilm.

Core-shell structure through conformal coatings with amorphous carbon and metallic coatings has been demonstrated an

efficient stragety to improve the excellent electrochemical performance[30-40]. However, upon the volume expansion of electrode, especially for the large-volume-variation electrodes, these coatings will fracture, leading to the loss of contract and the surface of the active maerials will still be exposed to electrolyte. Thus, more robust protection through coating for stress relieving is urgently needed to be constructed for more stable SEI layer in achieving long-cycle life[41-48].

Herein, to construct robust protection for large-volume-change materials, we rationally proposed a facile stragety for the fabrication of SnO_2-PPy nanofilm through hydrothermal treatment followed by subsequent electrodeposition. Unlike the core-shell structure, this kind of unique structure is able to possess the property integrating SnO_2 nanorod under the PPy film coverage wholly and ensuring steady and continuous contact between the PPy and SnO_2 nanrod array as well as the substrate, promising good cycling stability as anode for lithium battery. Our strategy is an optimized electrode with more flexible protective shell and more sustainable core-shell contact, yielding strain-relaxation and continuous electric contact simultaneously, with low weight percentage against active material.

Experimental

Synthesis of the bare SnO_2 nanorod arrays

The synthesis process is the same as the previous reported[46]. In a typical experiment, $SnCl_4 \cdot 5H_2O$ (0.73 g) and NaOH (1.25 g) were dissolved into 30 mL distilled water. After half an hour of magnetic stirring, 50 mg NH_4F was added into solution. The solution was transferred into a Teflon-lined autoclave (50 mL), in which a piece of cleaned nickel foam substrate was beforehand placed standing against the wall, heated to 200 ^oC for 24 h. The nickel foam acted as substrate for SnO_2 nanorod arrays during hydrothermal process. The as-deposited bare SnO_2 nanorod arrays were rinsed repeatedly with deionized water and dried at 60 ^oC for 8 h. The average mass of SnO_2 nanorod array (SnO_2 NA) is 1.67$\pm$0.35 mg/cm^2, which is calculated by the mass difference of the as-prepared samples before and after hydrothermal treatment.

Preparation of core-shell SnO_2-PPy NA, SnO_2-PPy nanofilm

Bare SnO_2 nanorod arrays were acted as the backbone for the growth of PPy shell. Electrolyte for electro-polymerization of PPy was 100 mM lithium perchlorate and 10 mM pyrrole monomer in acetonitrile solution. The electro-polymerization of PPy was carried out in a three-compartment system, using the bare SnO_2 nanorod arrays electrode as the working electrode, Ag/AgCl as the reference electrode and Pt foil as the counter electrode. The core-shell SnO_2-PPy nanorod array (core-shell SnO_2-PPy NA), SnO_2-PPy nanofilm was deposited by using a CHI760D electrochemical workstation through a constant current chronopotentiometry method at a current density of 1.6 mA/cm^2 for 700 s and 2000 s, respectively.

Characterization

The crystallographic information of the obtained products was measured with a Bruke D8 Discover X-ray diffraction (XRD) measurement using Cu Kα radiation in a coupled 2θ mode at room temperature. Field emission scanning electron microscopic (FESEM) images were carried out by JEOL-7100F. Energy dispersive X-ray spectra (EDS) were recorded by using Oxford EDS IE250. Fourier transformed infrared (FT-IR) transmittance spectra were recorded using the 60-SXB IR spectrometer. The electrochemical performance was characterized with coin cells of CR2016 type assembled in a glove-box filled with pure argon gas. Lithium foil was used as the anode, a solution of $LiPF_6$ (1 M) in EC/DEC (1:1 vol/vol) was used as the electrolyte, the as-prepared samples as cathode. Galvanostatic charge/discharge measurement was performed with a multichannel battery testing system (LANDCT2001A), cyclic voltammetry (CV) and electrochemical impedance spectroscopic (EIS) were measured by an Autolab Potentiostat Galvanostat at room temperature. Brunauer–Emmett–Teller (BET) surface areas were measured using a Tristar II 3020 instrument to measure the adsorption of nitrogen.

Details of finite element model simulation

FEM (Finite Element Model) simulation of the micromechanical behaviours of the free-standing SnO_2 NA, core-shell SnO_2-PPy and SnO_2-PPy film was carried out using ANSYS workbench to predict and identify the displacement/deformation of these nanostructures. In the simulation, the density, Young's modulus and Poisson ratio of the SnO_2 nanorod is set as 6.95 g/cm^3, 37.2 GPa and 0.21, respectively, and the density, Young's modulus and Poisson ratio of the PPy films is set as 0.97 g/cm^3, 3.6 GPa/cm^3, and 0.21, respectively. Free quad mesh is defined in all models. In our simulations, an isotropic initial stress of 0.1 MPa is applied in the domain of the nanorod to simulate the diffusion-induced stress resulting from the ion intercalating. The diameter of the nanorod is 100 nm.
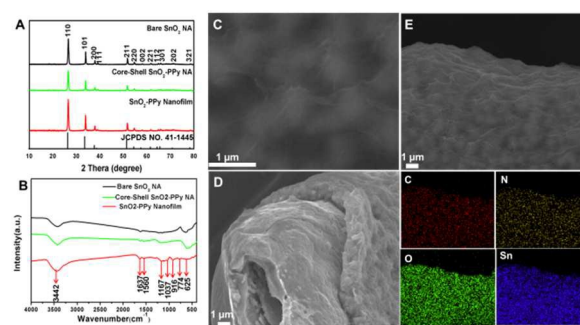
Results and discussion

Figure 2. (A) XRD patterns of bare SnO_2 NA, core-shell SnO_2-PPy NA, and SnO_2-PPy nanofilm; (B) FT-IR spectra of the bare SnO_2 NA, and SnO_2-PPy nanofilm; (C, D) SEM images of SnO_2-PPy nanofilm; (E) EDS element mappings of C, N, O and Sn, respectively.

Initially, XRD is carried out to investigate the crystal structure (Fig 2A). All the diffraction peaks of bare SnO_2 NA, core-shell

SnO$_2$-PPy NA and SnO$_2$-PPy nanofilm can be well indexed to the tetragonal rutile structure of SnO$_2$ (JCPDS NO. 41-1445). Four well-defined identified diffraction peaks at 26.5°, 33.8°, 37.8°, and 51.8° can be well assigned to (110), (101), (200), and (211) planes of tetragonal SnO$_2$. Moreover, there are no obvious differences among those three samples indicating that the electrodeposion process has no influence on the tin oxide array and no other peaks can be observed for PPy. Thus, to further identify the existence of PPy, FT-IR is carried out to test the bare SnO$_2$ NA and SnO$_2$-PPy nanofilm (Fig 2B). In these spectra, the bands in the range of 537–623 cm^{-1} were observed with bare SnO$_2$ NA, and SnO$_2$-PPy nanofilm can be assigned to the anti-symmetric and symmetric vibrations of Sn–O–Sn. The bands centred at 1637 and 1560 cm^{-1} for both the SnO$_2$-PPy nanofilm and the PPy correspond to typical C=C in plane vibration. In addition, the characteristic bands of deformation vibrations of the C–N stretching vibration of polypyrrole skeleton were found at 1167 and 1037 cm^{-1}, respectively. The band at 916 cm^{-1} can be assigned to C–H vibrations. Thus, these characteristic bands of PPy for both SnO$_2$-PPy nanofilm and PPy are nearly identical, except for the lower intensity observed with lower PPy content in the SnO$_2$-PPy nanofilm. The FT-IR results provide direct evidence that PPy is present in the SnO$_2$-PPy nanofilm. Furthermore, the morphologies of the as-prepared samples were characterized by SEM. The SnO$_2$ nanorods are initially captured by the small PPy nanosheet around the each side of the nanorod uniformly, forming core-shell SnO$_2$-PPy NA. Moreover, with increased deposition time, the PPy nanosheets grown on each SnO$_2$ nanorod interconnected, forming the SnO$_2$-PPy nanofilm. And the thickness of the SnO$_2$-PPy nanofilm is around 1μm (Fig 2D). To further estimate the existence of the PPy in the SnO$_2$-PPy nanofilm, the EDS elemental mapping is carried out. As can be observed in Fig 2E, the Sn, C, N, and O are uniformly distributed in the range of the image, indicating the evenly coated of the PPy, which is also confirmed by the semiquantitative EDAX results. Moreover, the mass of the PPy is 0.20±0.05 mg/cm^2, calculated by the mass difference of the as-prepared samples before and after electro deposition after drying at 70 ^{o}C for 24 h. which is 12% as high as that of the active material SnO$_2$ indicating the low density of the as-deposited PPy film.
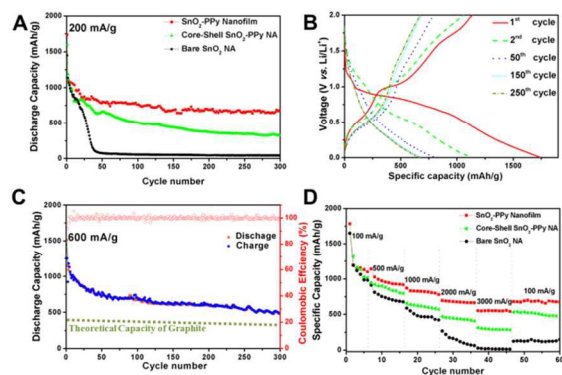
current density of 200 mAh/g; (B) galvanostatic charge−discharge curves of SnO$_2$-PPy nanofilm at the current density of 200 mA/g; (C) cycle performance of SnO$_2$-PPy nanofilm at high current density of 600 mA/g; (D) rate performance of bare SnO$_2$ NA, core-shell SnO$_2$-PPy NA, and SnO$_2$-PPy nanofilm.

Intrigued by the structural features of SnO$_2$-PPy nanofilm, coin cells (2016 type) of these samples are assembled by using lithium plate as anode at voltage range between 0.005 and 2 V to test the electrochemical performance at room temperature. Initially, the cycle performance at current density of 200 mAh/g is performed. The initial capacity of the bare SnO$_2$ NA, core-shell SnO$_2$-PPy NA, and SnO$_2$-PPy nanofilm is 1450, 1600, 1738 mAh/g, respectively, which is mainly contributed by the SnO$_2$ nanorod array (Fig. S9). During cycling, the capacity witnesses ups and downs, which results from the temperature variation of the seasonal changes and diurnal temperature difference. Despite this, the SnO$_2$-PPy nanofilm exhibits the most stable cycling performance resulting the 300th capacity of 701 mAh/g. The initial capacity fading may result from the irreversible reaction of the first process. Of all the three samples, the SnO$_2$-PPy nanofilm exhibits the most stable cycling stability. From 50 to 300 cycles, the capacity retention of SnO$_2$-PPy nanofilm is 87.5%, which is much higher than that of core-shell SnO$_2$-PPy NA(48.9%). The capacity of the bare SnO$_2$ NA is approaching below 100 mAh/g, making the definition of the capacity retention no sense. Further the current density is increased to 600 mAh/g, to identify the high-rate cycling stability. The capacity even after 300 cycles is 500 mAh/g, which is still well above the theoretical capacity of the graphite (372 mAh/g). Moreover, the columbic efficiencies, except for the first cycle, remain around 100%, indicating the stable SEI layer and excellent structural stability without electrolyte continuous decomposition.

Furthermore, the rate performance is investigated at different current densities of 100, 500, 1000, 2000, 3000, and back to 100 mA/g. As can be seen, the discharge capacities of the SnO$_2$-PPy nanofilm are 1099, 917, 777, 664, 512, and 691 mAh/g, respectively. Noticeably, even at high current density of 3 A/g, the capacity is 512 mAh/g, showing an excellent high-rate capacity. Moreover, the capacity at each current density is far higher than that of the bare SnO$_2$ NA, core-shell SnO$_2$-PPy NA. And even suffering from the high current density, the SnO$_2$-PPy nanofilm still retains good capacity and excellent cycling stability.
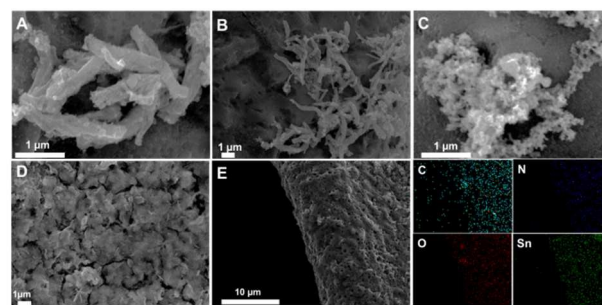

Figure 3. Electrochemical characteristics: (A) cycle performance of bare SnO$_2$ NA, core-shell SnO$_2$-PPy NA, and SnO$_2$-PPy nanofilm at

Figure 4. SEM images of core-shell SnO$_2$-PPy NA (A, B), SnO$_2$-PPy nanofilm (C, D) after cycling for 300 cycles at current density of 200

mAh/g; EDX mapping of SnO$_2$-PPy nanofilm (E) after cycling for 300 cycles at current density of 200 mAh/g.

Initially, in order to further identify that if the PPy nanofilm can act as a thin and robust protection, the SEM images of the bare SnO$_2$ NA, core-shell SnO$_2$-PPy NA and SnO$_2$-PPy nanofilm after 300 cycles is shown in. For the bare SnO$_2$ NA (Fig. S10), the SnO$_2$ nanorods can hardly be observed and moreover, many small pores are on the surface of it which can be attributed to the enormous volume variation during cycling. As for the core-shell SnO$_2$-PPy NA, there is also little active material left on it. But the nanorod turns out to show a very smooth surface which may be due to that the PPy still capture the nanorods steadily, indicating that the contact between core-shell SnO$_2$-PPy NA and the nickel foam is still easily lost, leading to poor cycling stability. However, unlike the bare SnO$_2$ NA, core-shell SnO$_2$-PPy NA, the SEM images of SnO$_2$-PPy nanofilm turn out to be almost the same with that before cycling. And there turns out many pores on the film which may result from the expansion of the SnO$_2$ nanorod. In order to further prove that if the SnO$_2$ nanorods are captured by the PPy, the EDX mapping is carried out, in which the element of C, N, Sn, and O is uniform distributed in the selected area, indicating the good contract between SnO$_2$-PPy nanofilm and the nickel foam even after long cycles. And the particles on surface may be the electrolyte that is dried during the SEM sample preparation. EIS spectra of the three different samples were carried out to provide insight of the kinetic (Fig. S3). The EIS spectrum shows two compressed semicircles from the high to medium frequency range of each spectrum, which describes the charge transfer resistance (R$_{ct}$) for these electrodes, and a line inclined at approximately 45° in the low-frequency range, which could be considered as Warburg impedance (Z$_W$) and has been fitted in this circuit, in which R$_1$ represents the Ohmic resistance of the electrode system, including the electrolyte and the cell components. R$_2$ and R$_3$ represent the resistance related to SEI and the charge transfer, respectively. CPE$_1$, CPE$_2$ and Z$_w$ are the capacitance related to SEI and the double layer and the Warburg impedance[49, 50], respectively. The values of R$_{ct}$ for the bare SnO$_2$ NA, core-shell SnO$_2$-PPy NA, and SnO$_2$-PPy nanofilm are 41, 70, and 92 Ω, respectively, suggesting fast kinetic for SnO$_2$-PPy nanofilm. Additionally, the slopes at low-frequency range are almost the same among the three different samples, suggesting the approaching ion diffusion rate. Besides, finite element method simulations were carried out and give insight in the deformation of the nanorod array in the bare SnO$_2$ NA, core-shell SnO$_2$-PPy NA, and SnO$_2$-PPy nanofilm. The initial stress was applied to simulate the diffusion-induced stress resulting from the ion intercalation. The migration modulus is calculated and plotted in each model and presented in Fig 5. The SnO$_2$ nanorod in the bare SnO$_2$ NA, core-shell SnO$_2$-PPy NA witnesses severe deformation and by integrating the conducting polymer coverage wholly, SnO$_2$ nanorods in SnO$_2$-PPy nanofilm witness the least deformation, indicating the most anti-pulverization property
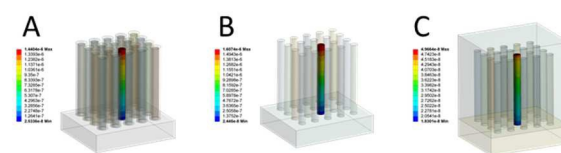

Figure 5. the calculated deformation contour for the bare SnO$_2$ NA (A), core-shell SnO$_2$-PPy NA (B), and SnO$_2$-PPy nanofilm (C).

Based on the results above, the SnO$_2$-PPy nanofilm exhibits outstanding cycling stability and high rate capability when compared with bare SnO$_2$ NA and core-shell SnO$_2$-PPy NA. This can be attributed to the unique structure, confining the SnO$_2$ nanorod array in the PPy coverage. Initially, integrating the conducting polymer coverage can provide a flexible confinement for anchoring each nanorod and maintaining the whole structural integrity and providing sustainable contract. Upon charging and discharging, the flexible conducting polymer PPy film can effectively act as a 'buffering' for accommodating severe stress resulting from volume expansion of SnO$_2$ nanorod, and avoid the aggregation of tin oxide nanorods. Besides, the thick PPy film is assembled by small nanosheets with pores which will not influence the contract between the active materials and the electrolyte, leading to fast lithium ion diffusion rate and effectively reducing the degree of the repeated formation/decomposition of SEI film. In addition, both the conducting polymer and the nick foam together provide continuous electron transport for the whole structure and more free space for fast charge and mass transfer, resulting in enhanced rate capability.

Conclusions

A facile and versatile strategy has been developed for fabricating the SnO$_2$-PPy nanofilm. When evaluated as anode for lithium battery, the SnO$_2$-PPy nanofilm exhibits the capacity retention of 87.5% from 50 to 300 cycles, which is much higher than that of core-shell SnO$_2$-PPy NA(48.9%), showing outstanding cycling stability and high-rate capability compared with the electrode of bare SnO$_2$ NA, core-shell SnO$_2$-PPy NA. The enhanced performance can be attributed to the reason that conducting polymer provides a flexible confinement for anchoring each nanorod and maintaining the whole structural integrity and offer a 'buffering' for accommodating and more free space for charge and mass transfer. An exploration and development of the multifunctional composite with conductive polymer have been developed, realizing the beneficial to fabricate new composite anodes with desired capacity, high-rate capability, and cycling stability. More significantly, this flexible PPy film holds the potential in severing as stretchy shell for conversion or alloying-based electrode materials or even being used in other fields, such as material protection, bionic design and drug delivery.

Conflicts of interest
All authors discussed the results and commented on the manuscript.
The authors declare no competing financial interest.

Corresponding Authors
*E-mail: mlq518@whut.edu.cn.
*E-mail: hel@whut.edu.cn.

Author Contributions
§ These authors contributed equally to this work.

Notes and references
1. P. G. Bruce, S. A. Freunberger, L. J. Hardwick, and J.-M. Tarascon, *Nat. Mater.*, 2011, 11, 19-29.
2. Y. M. Chiang, *Science*, 2010, 330, 1485-1486.
3. D. Larcher and J. M. Tarascon, *Nat. Chem.*, 2015, 7, 19-29.
4. K. Xu, *Chem. Rev.*, 2014, 114, 11503-11618.
5. M. N. Obrovac and V. L. Chevrier, *Chem. Rev.*, 2014, 114, 11444-11502.
6. D. Butler, *Nature*, 2007, 445, 586-588.
7. S. Chu and A. Majumdar, *Nature*, 2012, 488, 294-303.
8. D. Lindley, *Nature*, 2010, 463, 18-20.
9. Z. Peng, S. A. Freunberger, Y. Chen, and P. G. Bruce, *Science*, 2012, 337, 563-566.
10. P. Simon, Y. Gogotsi, and B. Dunn, *Science*, 2014, 343, 1210-1211.
11. P. L. Taberna, S. Mitra, P. Poizot, P. Simon, and J. M. Tarascon, *Nat. Mater.*, 2006, 5, 567-573.
12. A. Magasinski, P. Dixon, B. Hertzberg, A. Kvit, J. Ayala, and G. Yushin, *Nat. Mater.*, 2010, 9, 353-358.
13. A. R. Armstrong, C. Lyness, P. M. Panchmatia, M. S. Islam, and P. G. Bruce, *Nat. Mater.*, 2011, 10, 223-229.
14. N. Liu, H. Wu, M. T. McDowell, Y. Yao, C. Wang, and Y. Cui, *Nano Lett.*, 2012, 12, 3315-3321.
15. P. Senguttuvan, G. Rousse, H. Vezin, J. M. Tarascon, and M. R. Palacín, *Chem. Mater.*, 2013, 25, 2391-2393.
16. C. Wang, H. Wu, Z. Chen, M. T. McDowell, Y. Cui, and Z. Bao, *Nat. Chem.*, 2013, 5, 1042-1048.
17. L. Mai, Q. Wei, Q. An, X. Tian, Y. Zhao, X. Xu, L. Xu, L. Chang, and Q. Zhang, *Adv. Mater.*, 2013, 25, 2969-2973.
18. L. Mai, X. Tian, X. Xu, L. Chang, and L. Xu, *Chem. Rev.*, 2014, 114, 11828-11862.
19. L. Zhang, H. B. Wu, B. Liu, and X. W. Lou, *Energy Environ. Sci*, 2014, 7, 1013.
20. Y. Zhang, Y. Li, Z. Wang, and K. Zhao, *Nano Lett.*, 2014, 14, 7161-7170.
21. N. Liu, H. Wu, M. T. McDowell, Y. Yao, C. Wang, and Y. Cui, *Nano Lett.*, 2012, 12, 3315-3321.
22. Y. Zhao, J. Feng, X. Liu, F. Wang, L. Wang, C. Shi, L. Huang, X. Feng, X. Chen, L. Xu, M. Yan, Q. Zhang, X. Bai, H. Wu, and L. Mai, *Nat. Commun.*, 2014, 5, 4565.
23. J. Liang, X. Y. Yu, H. Zhou, H. B. Wu, S. Ding, and X. W. Lou, *Angew. Chem.*, 2014, 53, 12803-12807.
24. Y. Liu, N. Zhang, L. Jiao, Z. Tao, and J. Chen, *Adv. Funct. Mater.*, 2014, 25, 214–220.
25. K. Deng, H. Lu, Z. Shi, Q. Liu, and L. Li, *ACS Appl. Mater. Inter.*, 2013, 5, 7845-7851.
26. H. Tavassol, M. W. Cason, R. G. Nuzzo, and A. A. Gewirth, *Adv. Energy Mater.*, 2014, DOI: 10.1002/aenm.201400317.
27. G. A. Elia, J. Wang, D. Bresser, J. Li, B. Scrosati, S. Passerini, and J. Hassoun, *ACS Appl. Mater. Inter.*, 2014, 6, 12956-12961.
28. Q. Li, P. Wang, Q. Feng, M. Mao, J. Liu, S. X. Mao, and H. Wang, *Chem. Mater.*, 2014, 26, 4102-4108.
29. X. Zhou, Z. Dai, S. Liu, J. Bao, and Y. G. Guo, *Adv. Mater.*, 2014, 29, 3943-3949.
30. W. Chen, L. Qie, Y. Shen, Y. Sun, L. Yuan, X. Hu, W. Zhang, and Y. Huang, *Nano Energy*, 2013, 2(3): 412-418.
31. C. Guan, X. Wang, Q. Zhang, Z. Fan, H. Zhang, and H. J. Fan, *Nano Lett.*, 2014, 14, 4852-4858.
32. J. Qin, C. He, N. Zhao, Z. Wang, C. Shi, E.-Z. Liu, and J. Li, *ACS Nano*, 2014, 8, 1728-1738.
33. X. Zhou, Z. Dai, S. Liu, J. Bao, and Y. G. Guo, *Adv. Mater.*, 2014, 26, 3943-3949.
34. M. Yan, F. Wang, C. Han, X. Ma, X. Xu, Q. An, L. Xu, C. Niu, Y. Zhao, X. Tian, P. Hu, H. Wu, and L. Mai, *J. Am. Chem. Soc.* 2013, 135, 18176-18182.
35. Y. Yao, N. Liu, M. T. McDowell, M. Pasta, and Y. Cui, *Energy Environ. Sci.* 2012, 5, 7927–7930..
36. X. Fan, J. Shao, X. Xiao, X. Wang, S. Li, H. Ge, and L. Chen, *Nano Energy*, 2014, 9, 196-203.
37. Q. An, F. Lv, Q. Liu, C. Han, K. Zhao, J. Sheng, Q. Wei, M. Yan, and L. Mai, *Nano Lett.*, 2014, 14, 6250-6256.
38. D. Wang, Y. Zhao, X. Xu, K. M. Hercule, M. Yan, Q. An, X. Tian, J. Xu, L. Qu, and L. Mai, *Nanoscale*, 2014, 6, 8124-8129.
39. Y. Dong, S. Li, H. Xu, M. Yan, X. Xu, X. Tian, Q. Liu, and L. Mai, *Phys. Chem. Chem. Phys.*, 2013, 15, 17165-17170.
40. L. Zhang, K. Zhao, W. Xu, J. Meng, L. He, Q. An, X. Xu, Y. Luo, T. Zhao, and L. Mai, *RSC Adv.*, 2014, 4, 33332.
41. Y. Chen, S. Zeng, J. Qian, Y. Wang, Y. Cao, H. Yang, and X. Ai, *ACS Appl. Mater. Inter.*, 2014, 6, 3508-3512.
42. D. Chao, X. Xia, J. Liu, Z. Fan, C. F. Ng, J. Lin, H. Zhang, Z. X. Shen, and H. J. Fan, *Adv. Mater.*, 2014, 26, 5794-5800.
43. Y. W. Cheng, C. K. Lin, Y. C. Chu, A. Abouimrane, Z. Chen, Y. Ren, C. P. Liu, Y. Tzeng, and O. Auciello, *Adv. Mater.*, 2014, 26, 3724-3729.
44. Y. L. Ding, Y. Wen, P. A. van Aken, J. Maier, and Y. Yu, *Small*, 2014.
45. F. H. Du, B. Li, W. Fu, Y. J. Xiong, K. X. Wang, and J. S. Chen, *Adv. Mater.*, 2014, 26, 6145-6150.
46. W. Xu, K. Zhao, C. Niu, L. Zhang, Z. Cai, C. Han, L. He, T. Shen, M. Yan, L. Qu, and L. Mai, *Nano Energy*, 2014, 8, 196-204.
47. H. Zhao, Z. Wang, P. Lu, M. Jiang, F. Shi, X. Song, Z. Zheng, X. Zhou, Y. Fu, G. Abdelbast, X. Xiao, Z. Liu, V. S. Battaglia, K. Zaghib, and G. Liu, *Nano Lett.*, 2014, 14, 6704-6710.
48. R. Raccichini, A. Varzi, S. Passerini, and B. Scrosati, *Nat. Mater.*, 2014, doi:10.1038/nmat4170 .
49. Agnese Birrozzi, Rinaldo Raccichinib, Francesco Nobilia, Mario Marinaro, Roberto Tossici, and Roberto Marassi, *Electrochima. Acta*, 2014, 10, 228-233.

50. Raman Ravikumar and Sukumaran Gopukumar, *Phys. Chem. Chem. Phys.*, 2013, 15, 3712-3717.